Atmos. Chem. Phys. Discuss., 10, 8811–8859, 2010
www.atmos-chem-phys-discuss.net/10/8811/2010/

Atmospheric Chemistry and Physics Discussions

This discussion paper is/has been under review for the journal Atmospheric Chemistry and Physics (ACP). Please refer to the corresponding final paper in ACP if available.

Radiative forcing associated with a springtime case of Bodélé and Sudan dust transport over West Africa

C. Lemaître[1], C. Flamant[1], J. Cuesta[2], J.-C. Raut[1], P. Chazette[3], P. Formenti[4], and J. Pelon[1]

[1]Laboratoire Atmosphères, Milieux, Observation Spatiales, UMR 8190, CNRS and Université Pierre et Marie Curie and UVSQ, Paris, France
[2]Laboratoire de Météorologie Dynamique, CNRS, Ecole Polytechnique and ENS, Palaiseau, France
[3]Laboratoire des Sciences du Climat et l'Environnement, CEA, CNRS and UVSQ, Saclay, France
[4]Laboratoire Interuniversitaire des Systèmes Atmosphériques, CNRS and Université Paris Est Créteil Val de Marne/ Université Denis Diderot, Créteil, France

Received: 31 January 2010 – Accepted: 26 March 2010 – Published: 7 April 2010

Correspondence to: C. Lemaître (cyndie.lemaitre@latmos.ipsl.fr)

Published by Copernicus Publications on behalf of the European Geosciences Union.

Abstract

The radiative forcing due to mineral dust over West Africa is investigated using the radiative code STREAMER, as well as remote sensing and in situ observations gathered during the African Monsoon Multidisciplinary Analysis Special Observing Period (AMMA SOP). We focus on two days (13 and 14 June 2006) of an intense and long-lasting episode of dust being lifted in remote sources in Chad and Sudan and transported across West Africa in the African easterly jet region, during which airborne operations were conducted at the regional scale, from the southern fringes of the Sahara to the Gulf of Guinea. Profiles of heating rates are computed from airborne LEANDRE 2 and space-borne CALIOP lidar observations using two mineral dust model constrained by airborne in situ data and ground-based sunphotometer obtained during the campaign. Complementary space-borne observations (from MODIS) and in-situ observations such as dropsondes are also used to take into account a realistic infrared contribution of the water vapour. We investigate the variability of the heating rate on the vertical within a dust plume, as well as the contribution of longwave radiation to the heating rate and the radiative forcing of dust during the nighttime. The sensitivity of the so-derived heating rate is also analyzed for some key variables for which the associated uncertainties are quite large. During daytime, the warming associated with the presence of dust was found to be between 1.5 K day^{-1} and 4 K day^{-1}, on average, depending on altitude and latitude. Strong warming (i.e. heating rates as high as 8 K day^{-1}) was also observed locally in some limited part of the dust plumes. Obviously, during nighttime much smaller values of heating/cooling are retrieved (less than $\pm$1 K day^{-1}) but large enough to modify the low tropospheric equilibrium. Furthermore, cooling is observed as the result of the longwave forcing in the dust layer, while warming is observed below the dust layer, in the monsoon layer.

1 Introduction

The impact of dust on the climate system via the large uncertainties associated with the role of dust in the Earth's radiation budget is now widely recognized (e.g. Intergovernmental Panel on Climate Change, 2007). North Africa is the world's largest source of mineral dust. Satellite sensors consistently indicate that dust aerosol plumes are the most widespread, persistent and dense particulate contribution found on Earth (e.g. Prospero et al., 2002).

In the framework of the Bodélé Experiment (BodEx; Washington et al., 2006; Tegen et al., 2006), the SAharan Mineral dUst ExperiMent (SAMUM; Heintzenberg et al., 2009), and the African Monsoon Multidisciplinary Analysis (AMMA; Redelsperger et al., 2006), the impact of dust aerosols on the WAM dynamics (most notably via the aerosol "semi-direct" effect, i.e. the impact of aerosol-induced radiative warming on dynamics) has received increasing attention. Solmon et al. (2008) have investigated the climatic impact of shortwave and longwave radiative forcing of Saharan dust on the West African monsoon and Sahel precipitation using a regional climate model. They evidenced a reduction of monsoon intensity due to dust surface cooling, as well as an elevated heat pump effect in the higher troposphere induced by the dust diabatic warming. Heinold et al. (2008) have studied the mineral dust radiative effects and the feedbacks on the Saharan boundary layer meteorology by means of regional dust simulations for a one-week period in May 2006 using the regional dust model system LM-MUSCAT. They suggested that mineral dust modifies the stratification of the atmosphere and induce baroclinity.

Recently, Flamant et al. (2009) have investigated the structure of a dust plume travelling across West Africa with the African Easterly Jet (AEJ) during a major springtime dust event from the Bodélé region and Sudan using airborne lidar and dropsonde measurements, in June 2006. They hypothesized that the dust could impact on the radiation budget in the AEJ region and the structure of the AEJ itself (most notably via the aerosol "semi-direct" effect). Transport of massive amounts of dust in the AEJ from re-

ACPD
10, 8811–8859, 2010

mote eastern sources such as the Bodélé depression in northern Chad or the sources in west Sudan could impact on the atmospheric stratification in the AEJ region and, in turn, modify the properties of the AEJ itself, thereby possibly modifying the West African weather at the synoptic scale.

The objective of the paper is to provide reliable estimates of the radiative forcing at the regional scale (in both the short- and long-wave part of the spectrum) associated with the dust transported over the Sahel that can, in turn, be used to assess the impact of dust on the dynamic of the AEJ and African easterly waves. As a first step towards improved knowledge of the impact of the dust transported from the Saharan sources in the AEJ on the WAM dynamics, we aim at computing dust radiative forcing over the Sahel and Sudanian (i.e. sub-Sahel) regions, using a combination of novel remote sensing measurements and a radiative code. Based on a similar approach, Raut and Chazette (2008) have shown the benefit of using high vertical resolution measurements from lidar to assess precise aerosol-related radiative forcing, especially in the case of multi-layered aerosol plume.

The present study is conducted on 13 and 14 June 2006 on a dust event observed over Benin and Niger which originated from the Bodélé depression and from West Sudan (Flamant et al., 2009). Dust-related heating rate profiles are computed for a variety of atmospheric and surface conditions using high-resolution lidar measurements acquired from both airborne and space-borne platforms as well as the radiative code STREAMER (Key and Schweiger, 1998) in which we have implemented specific parameters representative of the area studied. This period was selected for several reasons: firstly, it occurred during a persistent large-scale transport episode of dust across West Africa (9–15 June 2006). Secondly, numerous airborne data (both in situ and remote sensing observations) were collected during the AMMA Special Observing Period (SOP, Lebel et al., 2010; June–September 2006). Thirdly, the airborne observations on 14 June were acquired at the time of and close to an A-Train overpass (including observations from the Cloud Aerosol Lidar and Infrared Pathfinder Satellite Observations – CALIPSO – among others, see Sect. 2).

This paper is divided into seven sections. Observations and related instruments are presented in Sect. 2, as well as flight operation. We introduce in Sect. 3 the radiative code and the optical properties of dust used. Section 4 deals with the analysis of the case studies of 13 and 14 June 2006, including meteorological conditions in which data were taken. Radiative impact is analyzed and results are discussed in Sect. 5, before concluding.

2 Data sources

2.1 Airborne data

During the AMMA SOP 1a (June 2006, see Lebel et al., 2010), the Service des Avions Français Instrumentés pour la Recherche en Environnement (SAFIRE) operated two research aircrafts, namely the Falcon 20 (F/F20) and the ATR 42. On 13 June 2006, the two aircrafts flew for a coordinated "north–south land-atmosphere-ocean interaction" mission over Benin, between Niamey (Niger) and Cotonou (Benin). In the afternoon of 14 June 2006, the two aircrafts flew between Cotonou and Niamey.

The aerosol vertical distribution together with the atmospheric dynamics and thermodynamics properties were documented at the regional scale using the airborne lidar LEANDRE 2 (Bruneau et al., 2001; Flamant et al., 2007) and dropsonde measurements along the meridian transects performed at 1.5° E on 13 June and between 2.15° and 2.5° E on 14 June, spanning from 15° N to 4° N (Fig. 1). The F/F20 was flying at 8000 m above mean sea level (msl). Operations were conducted between 11:30 and 13:30 UTC, and 13:00 and 15:00 UTC, on 13 and 14 June, respectively. Twelve dropsondes were released on 13 June and one on 14 June. Dropsonde data were processed with the Atmospheric Sounding Processing Environment software.

LEANDRE-derived total backscatter coefficient profiles (at 730 nm) were obtained from the atmospheric reflectivity profiles, via a standard lidar inversion technique (Fernald et al., 1972; Fernald, 1984), with a vertical resolution of 15 m and a horizontal

resolution of roughly 500 m. The molecular backscatter coefficient profiles used in the inversion procedure were obtained from dropsonde-derived pressure and temperature measurements. The aerosol backscatter-to-extinction ratio (BER) value used for the inversion is set to 0.02 sr^{-1} (Mueller et al., 2003; Tesche et al., 2009; Chazette et al., 2007) and is constant with altitude (e.g. Welton et al., 2000). The same value is used to derive aerosol extinction coefficient (AEC) profiles from the backscatter coefficient profiles in the present study. Furthermore, following Tesche et al. (2009), we assume the BER not to be wavelength dependent close to the source region of atmospheric desert dust.

The dust aerosol optical and radiative properties, as well as their vertical distribution were documented in situ in the lower troposphere using the AVIRAD aerosol sampling system (Formenti et al., 2010). It consists in an isoaxial and isokinetic inlet whose 50% passing efficiency has been estimated at 9 µm in diameter (Formenti et al., 2010). At the cruise speed of the ATR-42 (100 m s^{-1}) the delivered flow rate is 350 L m^{-1}. This allows connecting the inlet to multiple instruments in parallel. Seven straight sampling lines depart from the inlet to provide: (i) straight-levelled run averaged measurements of the particle absorption coefficient at 370, 470, 520, 590, 660, 880 and 950 nm (aethalometer model AE31, Magee Sci.), (ii) high-temporal resolution (1 s) measurements of the particle scattering and backscattering coefficients at 450, 550 and 700 nm (nephelometer model 3596, TSI Inc.); (iii) number size distribution between 0.3 and 20 µm in diameter (optical particle counter model 1.108, GRIMM), (iv) size-segregated aerosol composition and mass concentration by impactor sampling (4-stage Dekati impactors) and (v) bulk aerosol composition and mass concentration by on-line filter sampling on Nuclepore membranes. The in situ scattering and absorption coefficients and the number size distribution were used to (i) evaluate the relevance of the aerosol model used in the STREAMER radiative code (aerosol single scattering albedo and asymmetry factor), and (ii) to validate the lidar extinction coefficient retrievals performed for both LEANDRE 2 and CALIOP (Cloud Aerosol Lidar and Infrared Pathfinder Satellite Observations). State-of-the-art correction factors were applied to the scattering,

backscattering and absorption coefficient measurements (Anderson and Ogren, 1998; Weingartner et al., 2003). In the absence of a robust estimate of the refractive index, the number size distribution measured by the GRIMM optical particle counter are presented in terms of the equivalent diameter of the polystyrene latex spheres used for calibration (refractive index $\tilde{n} = 1.59–i0$).

On 13 and 14 June, the ATR42 flew patterns at a constant altitude of 700 msl (see Fig. 1), i.e. in the monsoon layer for the most part. It also performed two soundings, on both days and at both ends of the flight track (i.e. in the vicinity of Niamey and Cotonou), in which case it sampled the dust layer originating from the Bodélé depression as well as Western Sudan and subsequently transported with the AEJ across West Africa and over Benin.

Figure 2 shows a comparison between the LEANDRE-derived backscatter coefficient (at 730 nm, obtained via the so-called lidar inversion discussed above) and backscatter coefficient (ABC) retrieved at 700 nm from the AVIRAD system. The comparison is made for an altitude of 700 m. As shown in Fig. 2, a fair agreement is obtained between backscatter coefficient from AVIRAD and LEANDRE 2. Differences result essentially from attenuation of LEANDRE 2 signals. This comparison shows a minimum of the AVIRAD aerosol backscatter coefficient and of the LEANDRE 2 aerosol backscatter coefficient in the PBL at 10.1–10.3° N.

2.2 Space-borne observations

2.2.1 Aerosol distribution

The regional distribution of dust aerosols was described using three complementary satellite products. First, the Ozone Monitoring Instrument (OMI) daily Aerosol Index (AI) product was used. Second, aerosol optical depth (AOD) fields were obtained from the Moderate-resolution Imaging Spectroradiometer (MODIS) AQUA collection 005 over vegetated surfaces, and the MODIS/AQUA Deep Blue Collection 005 over desert surfaces (MOD08 product). Third, the vertical distribution of the aerosols was

documented using the space-borne lidar CALIOP (Winker et al., 2007) onboard the CALIPSO satellite. The three instruments are embarked on platforms (namely AQUA, CALIPSO and AURA for MODIS, CALIOP and OMI, respectively) that are part of what is now commonly referred to as the A-Train, and view the same scene within a few minutes. The A-train orbit overpasses West Africa twice a day, once during the daytime (between 12:30 and 14:30 LST – local standard time) and once during the nighttime (between 00:30 and 02:30 LST), and has a revisit time period of the same orbit of 16 days (Stephens et al., 2002).

The lidar CALIOP provides vertical profiles of atmospheric reflectivity (at 532 nm and 1064 nm) allowing the retrieval of the vertical distribution and the optical and radiative properties of aerosols and thin clouds. It has been previously used to study desert aerosols in the frame of AMMA program (e.g. Flamant et al., 2009; Kim et al., 2009). The CALIOP-derived reflectivity at 532 nm was analyzed along 2 overpasses (on 13 June around 01:39 UTC, 14 June around 13:20 UTC, see Fig. 1 for the position of the tracks).

CALIOP- derived total backscatter coefficient profiles (at 532 nm) were obtained from our own calculation (using level 1B version 2). The atmospheric reflectivity profile is retrieved using the same lidar inversion technique as for LEANDRE 2, with a vertical resolution of 60 m and a horizontal resolution of roughly 12 km. The molecular backscatter coefficient profiles used in the inversion procedure were obtained from molecular density profiles extracted from the National Centers for Environmental predictions (NCEP) analyses along CALIPSO tracks. The BER is set as varying with altitude to account for multiple scattering associated with the thick dust plume under scrutiny in the present case. We use a BER of 0.024 sr^{-1}, representative of dust particles (Kaufman et al., 2003). This ratio is modulated in the vertical by a multiple scattering coefficient increasing exponentially from 0.65 at the layer top, 0.87 below 500 m above ground level (a.g.l.) and to 0.95 at the ground, in agreement with the Monte-Carlo simulations of Berthier et al. (2006) and Young et al. (2008) or, as in Cuesta et al. (2009) and Messager et al. (2010). Sensitivity tests on phase function were made afterwards because

of uncertainties of this parameter.

2.3 Cloud properties

The presence of clouds underneath an aerosol layer can significantly modify the heating rates due to aerosols. Johnson (2003) has shown that presence of absorbing aerosol in stratocumulus-capped boundary layers led to large positive semi-direct radiative forcing, opposite in sign to the conventional direct forcing. For cumulus conditions, the semi-direct forcing was much smaller. Johnson et al. (2004) work on semi direct effect of aerosol evidenced cooling at the top of the atmosphere whenever absorbing aerosol resided above the cloud layer. When aerosols were located at the same level as the cloud, Johnson et al. (2004) show that this resulted in a strong heating.

Hence, cloud properties are necessary to estimate the effect of clouds. MODIS-derived cloud properties were also used as input to the streamer radiative code in order to compute aerosol radiative forcing above the shallow cumulus clouds commonly observed at the top of the monsoon layer over the southern half of Benin. The MODIS cloud product (MYD06_L2 collected from the AQUA platform) combines infrared and visible techniques to determine both physical and radiative cloud properties in the daytime as well as the nighttime. Daily global Level 2 data are used in this study, namely cloud phase (ice vs. water), effective droplet radius, and cloud optical thickness. These variables are available at 1-km resolution. Cloud top temperature, height, effective emissivity and phase as well as cloud fraction are also used and available at 5-km resolution. For the sake of homogeneity, 1-km resolution data were aggregated to form $5 \times 5\,\mathrm{km}^2$ pixels.

2.3.1 Earth surface characterization

The radiative forcing of aerosols strongly depends on the reflectivity of the underlying surface. As the albedo can vary significantly along a given track (ranging from 0.2

near the Gulf of Guinea coast region to almost 0.4 over parts of the Sahara), the evolution of the MODIS-derived albedo along the F/F20 and CALIPSO tracks was taken into account for the computation of the aerosol radiative forcing. In addition to the AOD and cloud properties related products, MODIS-derived surface albedo retrievals were also used in this study as input to the STREAMER radiative code. The MODIS albedo products (MCD43C3) used in this paper are the directional hemispherical reflectance (black-sky albedo) and bihemispherical reflectance (white-sky albedo). The MCD43C3 product contains 16 days of data provided in a level-3 data set projected to a $0.05^\circ \times 0.05^\circ$ grid. Both Terra and Aqua data are used to obtain this product, providing the highest probability for quality input data. The average of the black-sky albedo and white-sky albedo is provided as an input to STREAMER. The standard deviation on the albedo corresponding to the area of interest is about 0.025.

2.4 Ground-based observations

We also use observations of aerosol single scattering albedo and asymmetry factor at 441, 674, 869 and 1018 nm) derived from sun-photometer measurements acquired within the framework of the Aerosol Robotic Network (AERONET). The level 2.0 (cloud-screened) data from stations distributed over the Sahelian region, namely Banizoumbou (Niger; 13.54° N, 2.66° E), and the sub-Sahel, namely Djougou (Benin; 9.76° N, 1.6° E) and Ilorin (Nigeria; 8.32° N, 4.34° E) are used (see Fig. 1). Given that the AODs are larger than 0.5 at 440 nm in the present case, the error on the SSA is on the order of 0.03 (Dubovick et al., 2000).

3 The radiative code

Vertical profiles of aerosol radiative forcing over West Africa are quantified using the radiative transfer code STREAMER (Key and Schweiger, 1998; Key, 2001). STREAMER is a flexible code developed to compile radiances or fluxes for various atmospheric and

surface conditions. Calculations are made using a 2 stream scheme with a discrete ordinate (DISORT) solver. In the standard version, upward and downward fluxes (i.e. shortwave, longwave and net fluxes), cloud radiative effect ("cloud forcing"), and heating rates (HR) can be computed over 24 shortwave bands. We have added here 105 longwave bands, ranging from 20 to 35 710 cm^{-1}, with a spectral resolution of 20 cm^{-1}. In the present study, the radiative forcing (i.e. heating or cooling) is calculated from a pair of STREAMER simulations, i.e. as the difference between a dust-laden and a dust-free simulation. The total radiative forcing in the shortwave (longwave) part of the spectrum is computed as the integral of the forcing over the 24 (105) bands.

The aerosol optical properties (single scattering albedo, asymmetry parameter and the AEC) can be user defined. The single-scattering albedo (SSA) is defined as the ratio of the scattering coefficient to the AEC. The asymmetry parameter (g) is defined as the intensity-weighted average cosine of the scattering angle (the angle between incident light and scattering direction). The value of g ranges between −1 for entirely backscattered light to +1 for entirely forward scattered light. These parameters (especially the SSA) are critical, and one should note that these parameters are very sensitive to the mineral composition of dust and size distribution (Sokolik and Toon, 1999) and need adjustment to retrieve representative forcings (Balkanski at al., 2007). We have considered here two aerosol models in order to provide an estimate of the dispersion associated with the heating rate retrievals depending on the chosen aerosol model. The models were selected for their overall agreement with the data available on this case (airborne data and sun-photometers) in the visible. They are specified as a function of wavelength (Fig. 3).

The first dust model corresponds to the dust model prescribed in STREAMER, but modified following the study of Raut and Chazette (2008) in the visible part of the spectrum (between 0.2 and 0.7 µm) to account for the ultra-violet-visible complex refractive index, of dust particles observed in this part of Africa. This was determined from lidar measurements onboard an ultra light aircraft and the AERONET sunphotometer-derived size distributions gathered in Niamey during AMMA (January–February 2006).

In this model, the SSA, the asymmetry parameter and the AEC between 0.7 and 40 µm are prescribed according to the aerosol complex refractive index published by Voltz (1973). This model is here on referred to as the RaCH model.

The second model chosen is the more general "Alfaro I" model detailed in Chomette (1999) and Alfaro et al. (1998). Chomette (1999) derived the asymmetry parameter, SSA and AEC using a Mie model for spherical particles based on the refractive index of Voltz (1973) in the infrared (0.7 to 40 µm) and that of Grams et al. (1974) in the visible (0.2 to 0.7 µm). This model is referred to as the CHOM model in the following. Observations used in model RaCH have been made during the winter season, and aerosol properties may then be different from the ones observed in summer, as their origin may not be the same. The two selected models correspond to different compositions which are expected to induce a difference larger than the real one.

The single scattering albedo from the CHOM is seen to be overestimated (underestimated) with respect to the RaCH model at wavelength greater (less) than 0.7 µm (Fig. 3a, b). From Fig. 3b it is obvious that sun-photometer data are in better agreement with the RaCH model (resp. the CHOM model) for wavelength shorter (resp. larger) than 0.7 µm, thereby indicating the weakly absorbing nature of the dust aerosols sampled over the AERONET sites in Niger, Benin and Nigeria. The columnar SSAs derived from AERONET are ranging from 0.91 at 441 nm to 0.98 at 1018 nm. The AVIRAD derived SSA values exhibit more dispersion than their sun-photometer counterparts, especially on 14 June 2006. On 13 June, airborne SSA values are around 0.98, evidencing the presence of weakly absorbing aerosols. On 14 June, SSA values are smaller and exhibit a larger dispersion than on 13 June. This is thought to be due to the presence of biomass burning aerosols in the monsoon layer. For instance, localized peaks in carbon monoxide (in excess of 300 ppb) were observed over Benin along the ATR track on 14 June (not shown), while background carbon monoxide values on 13 and 14 were measured to be on the order of 200 ppb. It is worth noting that AVIRAD-derived SSA values are consistently showing better agreement with the model exhibiting the largest SSA. In conclusion, it appears that the aerosols in RaCH

are likely too absorbing across the visible spectrum. Likewise, the aerosols in CHOM are too absorbing below 0.8 µm and are in good agreement with observations between 0.8 and 1.1 µm.

The asymmetry factor from the two models is found in broad agreement between 1 and 2 µm, while it is seen to be underestimated in the RaCH model with respect to the CHOM model for the remaining part of the spectrum considered here (Fig. 3c, d). Between 0.3 and 1 µm, the sun-photometer derived asymmetry factor values are comprised between the curves associated with the two models (Fig. 2d). Observations indicate values of g between 0.72 and 0.77, in agreement with the values of Saha et al. (2008) and Raut and Chazette (2008). Figure 3e shows the spectral evolution of the modeled AEC (normalized at 550 nm), together with the AVIRAD measurements available in the visible. The normalized AEC in the RaCH model is underestimated (overestimated) with respect to the CHOM model for wavelengths larger (smaller) than 550 nm. AVIRAD data are in broad agreement with the modeled AEC. Finally, the real refractive indices used in RaCH and CHOM are very similar but imaginary parts are not, reflecting SSA differences (Fig. 3f).

Gaseous absorption by water vapour, carbon dioxide, ozone, and oxygen is computed following Tsay et al. (1989). The model runs with an emissivity of 0.90 for desert surfaces (Ogawa and Schmugge, 2004) and of 0.85 for the oceanic surfaces. The spectral reflectance is taken according to Tanré et al. (1986) for desert and from Briegleb et al. (1986) for oceanic surfaces. Profiles of atmospheric temperature, water vapor, and pressure need to be prescribed as inputs to the STREAMER simulations.

4 The 13–14 June 2006 case study

4.1 Synoptic conditions during the dust event

During the 9–12 June period, i.e. 2–4 days before the airborne observations over Benin, strong northeasterly Harmanttan winds were seen in the European Centre for Medium-

range Weather Forecast (ECMWF) analyses over the Niger-Chad-Sudan sector of the Sahara (not shown). These winds were the primary driver of dust emission in this sector, known to hold some of the most productive dust sources in West Africa, notably the Bodélé depression (in Chad) and the Sudanese sources in the May–July period. The ECMWF analyses at 925 hPa show strong winds, in the form of a northeasterly low-level jet, to the east of West Sudan at 00:00 UTC during the 9–13 June period (Flamant et al., 2009). Similarly, strong north-easterly low level winds were also observed between the Tibesti and Ennedi mountains in Chad, and over the Bodélé depression at 00:00 UTC. It is now well established that dust emission from the Bodélé (and also over Sudan in this case) are related to the downward transfer of momentum from the nocturnal low-level jet to the surface due to turbulent mixing after solar heating commences each day (Todd et al., 2008).

The transport patterns of dust from eastern Saharan sources towards the southwest in this case have been described by Flamant et al. (2009). In particular, they have highlighted the role of the inter-tropical discontinuity and the Darfur Mountains in injecting the aerosols from Bodélé and Sudan, respectively, over the monsoon flow, and in the AEJ region.

4.2 Regional distribution of aerosol from 9 to 13 June 2006

The temporal evolution of the dust load over the Bodélé region and over Sudan has been investigated by Flamant et al. (2009) using daily MODIS Deep Blue AODs between 9 June and 15 June 2006. They show that over the Bodélé region, the dust load exhibited a decrease from 2.6 to 0.65 between 9 and 13 June, while over Sudan the dust load increased between 9 and 12 June (from 0.70 to 1.1), and decreased afterward. As noted by Flamant et al. (2009), the aerosol load appears to be advected westward between 9 and 14 June (not shown).

Figure 4a shows the regional distribution of AOD on 13 June. The dust transport from the Eastern dust sources across West Africa with the AEJ is seen in the form of an elongated band of high AOD values (>1 at 550 nm) extending from Sudan to Senegal

between roughly 5° and 18° N. The dust load over Benin on 14 June (~0.5–1.2) was observed to be smaller than on 13 June (~1.5–1.6) (Fig. 4b). This is in agreement with Flamant et al. (2009) who have shown that in Djougou, AERONET-derived AOD values at 440 nm (675 nm) decreased from 1.12 (1.06) at midday on 13 June to 0.72 (0.66) at midday on 14 June.

4.3 Vertical distribution of dust over Benin on 13 and 14 June

The two-dimension cross-sections of attenuated backscatter coefficient ABC (AEC) retrieved from LEANDRE 2 along the F/F20 flight track on 13 June and 14 June are shown in Fig. 5a and c (Fig. 5b and d), respectively.

On 13 June, LEANDRE 2 measurements evidenced the presence of an extended and thick dust plume spanning from north of Niamey (15° N) to the Benin coastline (6° N) (Fig. 5b). The depth of the plume was of the order of 3 km, while the height of the top of the plume was observed to increase with latitude. In connection with the presence of the monsoon flow, smaller reflectivity values were observed below the dust plume along the entire transect, because of the much lower aerosol content to which the lidar is sensitive. South of 11° N, over the continent, cumulus clouds were observed below the dust plume which marked the top of the monsoon layer. They are characterized by large AEC values, in excess of 0.5 km^{-1} In some instances, these clouds were observed to penetrate the dust plume (e.g. between 8° and 9° N). The dust plume over Benin and Niger is characterized by values in excess of 0.15 km^{-1}. Values larger than 0.4 km^{-1} are also seen in the vicinity of Niamey (from 12.5° to 15° N), between 2.5 and 3.5 km m.s.l.

On 14 June, north of 6.5° N, the LEANDRE 2-derived AEC along the transect exhibits lower values than on the previous day above the monsoon flow (Fig. 5d). The largest AEC values on this day are on the order of 0.15 km^{-1}. The latitudinal structure of the altitude of the plume top on 14 June was very similar to that observed on 13 June. However, it was observed to extent further south. Also, north of 10° N, the AEC was observed to exhibit much less vertical variability. Numerous cumulus clouds were also

observed at the top of the monsoon layer over the southern part of the transect. As pointed out by Flamant et al. (2009), the reduction of the dust load between 13 and 14 June is essentially related to the fluctuations of the dust emissions over the source regions 2 to 4 days prior to the airborne measurements over Niger and Benin. The comparison between the LEANDRE-derived AODs (obtained after integration of the AEC in the dust plume using a BER of 0.20 sr^{-1}) and the MODIS AODs at 670 nm along the F/F20 track the 14 June 2006, without clouds, is shown in Fig. 5e. MODIS AODs are consistent with lidar AODs in the plume. It is observed that the latitudinal trend in MODIS AODs is more marked to the South. The lower lidar AODs are partly explained by the larger wavelength.

5 Radiative impact

A series of STREAMER simulations were performed on 13 and 14 June 2006, to quantify radiative forcing profiles of dust aerosols according to the latitude (between 6° N to 15° N) between the vegetated coast and the dry Sahel.

First, STREAMER simulations are performed for each airborne and space-borne lidar-derived AEC profile to infer the radiative forcing (i.e. heating or cooling) associated with the dust-laden atmosphere. In addition to the lidar-derived AEC profiles, profiles of temperature, pressure and water vapour mixing ratio as well as surface albedo have to be provided. MODIS-derived surface albedo (0.05° resolution) was linearly interpolated along the F/F20 and CALIPSO tracks so that one albedo value is associated with a given AEC. In the case of the presence of a low-level clouds, such as the cumulus clouds seen in the lidar observations at the top of the monsoon layer (Fig. 5), the radiative forcing is computed at the level of the cloud layer and above the cloud top height, accounting for the cloud properties as derived from MODIS (see Sect. 2.2.2). We have used average cloud properties as representative of cumuli over southern Benin. The following MODIS-derived values have been used as characteristic of the cloud properties in the region of interest: the cloud optical thickness in the visible is taken as

7.25 (±6.63), the cloud particle effective radius is set to 7.74 (±3.80) µm and the liquid water concentration is equal to 0.051 (±0.045) g m^{-3}. We only consider low-level liquid-water clouds (high-level or even mid-level clouds being almost always above the aerosol plume). The cloud top temperature is determined from the MODIS-derived cloud top pressure and a prescribed temperature profile. The cloud thickness is computed in STREAMER using the values of optical thickness, effective radius and water concentration. In the case of elevated clouds such as towering cumuli reaching the top of the aerosol layer (see for instance at 13.3° N in Fig. 5a and b) the profile is discarded altogether. There are very few such cases in the LEANDRE 2 data. Similarly, elevated clouds (such as cirrus clouds) associated with nearby convective systems were often observed with CALIPSO. In the cases also, the contaminated profiles are discarded altogether. Finally, the profiles of temperature, pressure and water vapour mixing ratio profiles needed to compute the radiative forcing from the CALIOP data are from NCEP analyses and are provided for each CALIOP profile. On the other hand, we have used dropsonde measurements to characterize the lower troposphere and compute the radiative forcing. STREAMER simulations on 13 June are performed using average temperature, pressure and water vapour mixing ratio profiles computed from the profiles obtained from the 13 dropsondes released on that day. STREAMER simulations on 14 June are performed using the temperature, pressure and water vapour mixing ratio profiles obtained from the single dropsonde released on that day. As discussed in the next section, radiative forcing in these cases was only marginally sensitive to the temperature, pressure and water vapour mixing ratio profiles.

Figure 6 shows an example of an AEC retrieved from the LEANDRE 2 measurements in cloud-free conditions over Benin at 10° N (Fig. 6a) and the corresponding vertical profile of radiative heating obtained from STREAMER using the RaCH model and CHOM model (Fig. 6b). In this example, the dust layer traveling the AEJ region is essentially comprised between 1.8 and 4.8 km a.g.l. Below, the AEC decreases and is minimum around 1 km a.g.l., and increases in the monsoon layer. Furthermore, the examination of the spectral dependence of the in situ measured scattering coefficient

show that mineral dust was indeed dominant north of 10° N. Figure 6 also shows an example of an AEC profile retrieved from LEANDRE 2 in the presence of low-level clouds over the Gulf of Guinea at 5° N (Fig. 6c) and the corresponding vertical profile of radiative heating obtained from STREAMER using the RaCH model and CHOM model (Fig. 6d). In the present case the altitude of cloud is 2.3 km.

The AEC profile shown in Fig. 6a was obtained using a BER of 0.02 sr^{-1}, and the heating rate profiles (Fig. 6b) were obtained using a visible surface albedo of 0.25, a temperature profile derived from the dropsonde released on 13 June at 10° N, a mean ozone column of 320 Dobson, and over a vegetated surface. This profile is referred to as the "reference" profile in the following. The maximum heating rate of about 2.3 K day^{-1} is obtained at the altitude where the dust plume exhibits the largest AEC values (i.e. 3 km m.s.l.) for RaCH model and about 3 K day^{-1} with CHOM model. Satheesh et al. (2002) evidenced a dust-related heating rate between 0.4 and 1.2 K day^{-1} over northern Africa (10° N–20° N; 20° E–30° E) and southern Africa (10° S–20° S; 20° E–30° E) using direct observation of solar radiation in the shortwave part of the spectrum. From Fig. 6a and b, it is quite obvious that the heating rate increases as AEC increases, even in the monsoon layer.

The AEC profile shown in Fig. 6c was obtained using a BER of 0.02 sr^{-1}, and the heating rate profiles (Fig. 6d) were obtained using a cloud optical thickness in the visible of 7.25, a cloud physical thickness of 45 m, a cloud particle effective radius of 7.74 µm, a liquid water concentration equal to 0.051 g m^{-3}, a temperature profile derived from the dropsonde released on 13 June at 10° N, and a mean ozone column of 320 Dobson. This profile is referred to as the "reference" profile in cloudy conditions in the following. In these conditions, the heating rate just above the cloud layer can reach 4.3 K day^{-1} (RaCH model) and 4.8 K day^{-1} (CHOM model) for an AEC of 0.08 km^{-1}, while lower heating values are obtained in cloud-free conditions at higher altitude where the AEC reaches 0.17 km^{-1} (2.8 and 3.2 K day^{-1} for the RaCH and CHOM models, respectively). This is found in agreement with the large-eddy model based results of Johnson et al. (2004) who evidenced the strongest heating rates to be located in the

vicinity of clouds. In the case, nonlinear effects are evident in the immediate vicinity of the clouds, and the strongest heating rates are obtained for significant but yet moderate AEC values.

5.1 Sensitivity studies

In this section we conduct a series of sensitivity studies to (i) the surface albedo, (ii) type of soil (vegetated or rather dry), (iii) aerosol backscatter-to-extinction ratio, (iv) ozone content, (iv) temperature and water vapor mixing ratio profiles, as well as (v) cloud microphysical, optical and structural properties, in order to evaluate the potential sources of uncertainties in the radiative forcing results presented above. The sensitivity analyses are conducted using the AEC profiles shown in Fig. 6a (cloud-free conditions) and Fig. 6c (low-level cloud conditions), and for the RaCH aerosol model. The sensitivity is also quantified in terms of error profiles, which are computed as the difference between the "reference" profile (shown in Fig. 6b and d) and "sensitivity" profile, divided by the "reference" profile.

5.1.1 Cloud-free conditions

The first sensitivity test was conducted on surface albedo. While changing the albedo from 0.15 to 0.25 (all other variables remaining constant), the heating rate profile is only slightly modified and is shifted towards higher values as albedo increases (Fig. 7a). A surface albedo increase means that more radiation is reflected by the surface. The outgoing radiation leaving the surface also interacts with dust layer which increases the overall absorption. This result is in agreement with Heintzenberg et al. (1997), Satheesh (2002) or Raut and Chazette (2008). As a result, an error of 40% on the albedo leads to heating rate differences as large as 0.3 K day^{-1} (Fig. 7a) in the part of the plume exhibiting the largest AEC (and smaller elsewhere). This leads to an error on the heating rate profile (nearly constant with height in the aerosol layer) on the order of 15% and a slightly smaller error in the monsoon layer (Fig. 7e).

The sensitivity of the heating rate retrievals to the type of surface was also investigated by performing a STREAMER simulation with the surface characterized as "vegetation" and another with a soil characterized as "dry" (all other variables being identical). The radiative impact of dust is strongest above vegetated (darker) surfaces (Fig. 7b) consistently with the change in albedo discussed previously. The difference between the surface type leads an error on the order of 10% on the heating rate profile in the aerosol layer and a slightly smaller error in the monsoon layer (Fig. 7e).

Profiles issued from dropsondes released on 13 June every 2° along the Niamey-Cotonou transect were used to compute the heating rates at 10° N on 14 June. The sensitivity of the heating rate retrievals to the temperature, pressure and water vapor mixing ratio profiles is shown in Fig. 7c to be negligible, except below the dust layer where it is very small between 0 and 0.2 K day^{-1}.

Concerning ozone, heating rate profiles were found not to be sensitive to the total column (not shown). The sensitivity was tested for a value of 280 Dobson.

Finally, we have tested the sensitivity of the heating rate profiles to the BER value. As stated in Sect. 2.1, a value of 0.02 sr^{-1} was selected for the inversion of the LEANDRE 2 data, while a value of 0.024 sr^{-1} (modulated by a factor accounting for multiple diffusion and ranging between 0.95 and 0.65) was chosen for the inversion of the CALIOP data (Sect. 2.2.1). Hence, we have analyzed the sensitivity of the LEANDRE 2 – derived heating rates to BER values of 0.025 and 0.03 sr^{-1}. An increase of the BER leads to a decrease of heating rate values throughout the profile (Fig. 7d). Errors resulting from uncertainties on the BER can be as high as 60% for a BER of 0.03 sr^{-1} in agreement with the results of Berthier et al. (2006). The highest errors are found in the monsoon layer, i.e. below the dust plumes.

5.1.2 Cloudy conditions

We have tested the sensitivity of the heating rate profiles to the BER values, as in the previous section. As observed for the cloud-free profiles, increased BER values lead to decreased heating rate values throughout the profile (Fig. 8a). Resulting errors are

comprised between 15 and 35% for a BER of 0.025 sr^{-1} and between 30 and 50% for a BER of 0.03 sr^{-1} (Fig. 8e). As cloud-free condition, heating rate profiles were found not to be sensitive to the total column values prescribed in STEAMER (not shown).

The sensitivity of heating rates to the cloud radiative, optical and structural properties were then tested for: (i) cloud physical thickness (Fig. 8b), (ii) cloud optical depth (Fig. 8c), and (iii) cloud particle effective radius (Fig. 8d) . Heating rates profiles were found to be insensitive to water concentration (not shown). Sensitivity tests were made based on the standard deviation of the MODIS-derived clouds properties.

The influence of the cloud physical thickness on the heating rate profiles is mainly located in the immediate vicinity of the cloud layer (Fig. 8b). The maximum of heating rate in the cloud is found to be weaker for the shallower cloud (i.e. 10 m). The maximum is found to be located higher because the reference of physical thickness is at the top of the cloud. The error relative to the reference value (45 m) is null in most of the aerosol layer (Fig. 8e) and is more important in the lower part of the plume, in the cloud layer. The error is largest for the smallest cloud physical thickness reaching a value in excess of 100% for a very shallow cloud and on the order of 25% for the thicker cloud.

The sensitivity of the heating rate profiles to the cloud optical thickness values is analyzed next for extreme values ranging from 1 to 14.95 (Fig. 8c). An increase of the optical thickness leads to an increase of heating rate values throughout the profile. Important errors are also found at the bottom of the dust layer, in the vicinity of the cloud top. They are smaller for optically thicker clouds (35% for an optical depth of 14.95 versus 100% for an optical depth of 1). In the core of the dust plume, the errors are on the order of 20% for optically thick clouds and 35% for optically thin clouds.

Finally, the sensitivity of the heating rate retrievals to the cloud particle effective radius was found to be quite small (Fig. 8d). Important errors are also found at the bottom of the dust layer, in the vicinity of the cloud top. They are smaller for smaller effective radius. In the core of the dust plume, the errors are on the order of 5% or less.

We have to bear in mind that a cooling effect at the level of the cloud is observed for a “reference case”, without aerosols. The previous results highlight that a dust

aerosol layer overlying a cloud reduces the cloud cooling effect mentioned above. This is due to an attenuation thought the dust layer of the radiative fluxes reaching the cloud. In comparison to the "reference case" the resulting effect is a local warming of the atmosphere at the cloud location.

5.2 Daytime observations

5.2.1 Radiative impact from LEANDRE 2 data

Figure 9a and b show the heating rates HRs associated with dust on 13 June computed using the RaCH and CHOM models, respectively, and the AEC shown in Fig. 5b. Figure 9d and e represent the HR associated with dust on 14 June 2006 computed using the RaCH and CHOM models, respectively, and the AEC shown in Fig. 5d.

Maximum values of the heating rates are observed at the location of maximum dust-related AEC. They are mainly due to the shortwave contributions (for more than 60%). Two regions of particularly high heating rates (in excess of $6\,K\,day^{-1}$, reaching $8\,K\,day^{-1}$ in some instances, see Fig. 10) are seen between 6° N and 10° N (above the cumulus clouds over vegetated Benin) and between 12° and 15° N (over the drier Sahel). A weak but non negligible HR (on the order of $1\,K\,day^{-1}$) is observed in the monsoon layer. HRs in excess of $2\,K\,day^{-1}$ (resp. $3\,K\,day^{-1}$) are generally observed to be associated with the thickest part of the dust plume using the RaCH (resp. CHOM) model. The difference between the HRs obtained with the CHOM and RaCH models on 13 June can reach values as large as $3\,K\,day^{-1}$ (Fig. 9c). The higher HRs retrieved with the CHOM model likely reflect the fact that the dusts in this model are characterized by lower SSA values in the visible (Fig. 3c, d). On 13 June, the average heating rate difference in the dust layer is about $1\,K\,day^{-1}$.

On 14 June, the heating rates derived from the RaCH model (Fig. 9d) and CHOM model (Fig. 9e) are smaller than on 13 June. Differences in heating rates between the two days are on the order of several $K\,day^{-1}$ and are most significant north of 12° N (Fig. 10). On 14 June, the highest heating rates are seen in the form of a thin layer

between 7° and 10° N, mostly above the cumulus clouds covering southern Benin. On 14 June, the average heating rate difference in the dust layer is about 0.7 K day^{-1} (Fig. 9f).

5.2.2 Radiative impact from CALIOP data

The same procedure is followed to quantify the radiative impact of dust using data gathered by CALIOP. Results are presented in Fig. 11 for the daytime CALIPSO track on 14 June. The HRs corresponding to the CALIOP AEC cross-section is shown for both the RaCH model (Fig. 11b) and the CHOM model (Fig. 11c). Finally, the difference between the HRs retrievals from the two aerosol models is shown in Fig. 11d. The black areas correspond to regions located below clouds were calculation cannot be done since the reflectivity signal is strongly impacted by clouds or totally attenuated. The radiative forcing in the dust plume is observed to be in excess of about 2 K day^{-1} in the region located between 3 and 5 km altitude from 6 to 35° N (Fig. 11b, c). The strongest HRs are observed to be on the order of 3 to 4 K day^{-1}, i.e. slightly less than what was observed by LEANDRE 2 for instance in the region between 6 and 15° N. In particular, CALIOP seems to be missing the thin layer of high HR values observed by LEANDRE 2 around 3 km m.s.l. between 6 and 10° N (also see Sect. 5.2.3). The difference between the HRs derived from the two aerosol models is about 0.8 K day^{-1} on average in the dust layer and can reach 2 K day^{-1} locally, particularly above the cumulus clouds over southern Benin, as observed with LEANDRE 2. In this case also, the difference in HRs observed with the CHOM model are caused by the more absorbing dust properties of this model with respect to the RaCH model.

5.2.3 Comparison of results obtained with LEANDRE 2 and CALIOP

Vertical cross section of AEC and radiative HRs deduced from LEANDRE 2 and CALIOP AEC profiles show coherent results. In both datasets, the maximum heating rate is located between 6° N and 15° N as well as between 2 and 5 km m.s.l., i.e.

in the AEJ which was shown by Flamant et al. (2009) to extend from 5° to 14° N and between 2 and 5 km m.s.l. over Benin and southern Niger (Fig. 12).

In spite of good agreement between the LEANDRE 2 and CALIOP heating rate retrievals, the latter were always observed to be greater than the former, except in the monsoon layer. As an example, Fig. 12a shows the vertical profile of the AEC at 12° N for the two instruments and the corresponding vertical profile of the HR at the same latitude (Fig. 12b). The AEC profiles are seen to be in good agreement in the upper part of the dust layer (between 2 and 5 km a.g.l.) and to be somewhat different below 2 km a.g.l. The difference below 2 km a.g.l. is related to the correction of the attenuation in the lidar inversion technique discussed in Sect. 2. Given that LEANDRE 2 measurements were acquired from a much lower altitude and just above the dust plume, the signal-to-noise ratio (20) is much greater than for CALIOP (~1 at 532 nm and at night, for an horizontal resolution of 1 km and a vertical resolution of 60 m) which enables a better correction of the dust-induced attenuation (assuming an unbiased BER value) and to obtain more realistic backscatter and AEC values in the monsoon layer below the dust layer.

The HR is slightly greater for CALIPSO (+0.2 K day^{-1} on average for the profile) than for LEANDRE. However, in some instances, the difference between the two profiles can reach 0.5 K day^{-1} as for example below the dust layer, in the monsoon layer (Fig. 12b).

A profile-to-profile comparison between HRs retrieved with CALIOP and LEANDRE is shown in Fig. 12c. For the comparison, approximately 10 LEANDRE 2 profiles were averaged together to match the spatial resolution of CALIOP. Only HR values in the dust plume (between 2 and 5 km a.g.l.) and in excess of 0.15 K day^{-1} are concerned here. Overall, we find a marked tendency for CALIOP-derived HRs to be overestimated with respect to the LEANDRE-derived heating rates (see regression line in Fig. 12c). Nevertheless, there is a fair agreement between the CALIOP-derived and LEANDRE-derived HRs for values comprised between 0.5 and 3 K day^{-1}. The correlation coefficient between the CALIOP- and LEANDRE-derived heating rate is around 0.85.

ACPD
10, 8811–8859, 2010

5.2.4 The importance of radiative forcing in the infrared during daytime

In this study, the contribution of the HR in the infrared is accounted for. Generally only HRs in the visible part of the spectrum are considered (e.g. Saha et al., 2008, Dubovik et al., 2002, Satheesh et al., 2006) since the contribution of longwave is supposed to be negligible. Nevertheless, during the SHADE campaign, Highwood et al. (2003) evidenced a warming at the surface (up to 0.5 K day^{-1}) and a cooling within a Saharan dust plume (up to 0.5 K day^{-1}) in the infrared, over the Atlantic Ocean.

The contribution of the radiative forcing in the longwave (0.7 to 400 µm) and shortwave (0.2 to 0.7 µm) parts of the spectrum to the total radiative forcing is shown at two locations along the F/F20 transect (10° N in Fig. 13a; 13° N in Fig. 13b). The contribution of the forcing in the infrared is observed to be on the same order of magnitude as the contribution in the visible. In some instances, (i.e. at 10° N, Fig. 13a), the impact in the infrared is more important than in the visible, as for example below the dust plume and in the monsoon layer. In the dust plume, the HR is observed to be stronger in the visible than in the infrared. Nevertheless, the contribution in the infrared is on the order of 40% (Fig. 13c, d).

The mean contribution of the radiative forcing in the infrared was investigated along transect (Fig. 13e). It can reach 75% near the surface and decreases with altitude. On average, the contribution of the infrared to the heating rates in the dust plume is on the order of 40%.

5.3 Nighttime observations

Estimating dust related HR during the nighttime is essential to fully understand the radiative impact of the dust transported in the AEJ region across West Africa on the monsoon dynamics. Because such dust transport episodes can last for a few days and nights, and because the radiative impact of the advected dust will be likely be different whether dust interact with longwave and shortwave radiations or just longwave radiations, the effect on the atmospheric dynamics is expected to be different.

The radiative impact of the dust plume from Eastern Africa was also investigated using nighttime CALIOP data over Ghana, Bukina-Faso and Niger (Fig. 1a). In the early hours of 13 June, a distinct dust plume was observed 8° and 15° N, and between 2 and 4.5 km m.s.l. (Fig. 14a). A thin layer of aerosol was also observed south of 8° N at about 3 km m.s.l. The radiative impact of dust during the night is quite different from that observed during the day, because of the contribution of the infrared only (Fig. 14b, c). In this case, a radiative cooling on the order of 0.2 to 0.8 K day^{-1} is retrieved in the dust layer, while a warming is seen below the dust layer (0.2 and 0.6 K day^{-1}). These results are in agreement with the findings of Stone et al. (2007), Mohalfi et al. (1998) and Highwood et al. (2003). Furthermore, the radiative impact derived from the RaCH model (Fig. 14b) and the CHOM model (Fig. 14c) are identical (not shown), even though the two models exhibit discrepancies in the longwave part of the spectrum in terms of SSA (Fig. 3a), asymmetry factor (Fig. 3c) and AEC (Fig. 3e). This suggests that the heating rate in the infrared is not very sensitive to the aerosol model (RaCH or CHOM).

6 Summary and conclusion

The present study has evaluated a new approach to quantify the radiative impact of dust from airborne LEANDRE 2 and space-borne CALIOP lidar observations using a two mineral dust models constrained by airborne in situ data and ground-based sun-photometer. Complementary space-borne observations (from MODIS) and in-situ observations such as dropsondes are also used. The sensitivity of the so-derived heating rate is also analyzed for some key variables for which the associated uncertainties are quite large.

We demonstrate the benefit of lidar-derived AEC to determine the HR profiles. This is particularly crucial if one wants to thoroughly understand the radiative forcing feedback on atmospheric boundary-layer dynamics. Furthermore, we have analyzed the contribution of the forcing in the longwave part of the spectrum during the daytime and

the nighttime. This is essential if one wants to fully understand the radiative impact of the long-lasting dust episodes transported in the AEJ region across West Africa on the monsoon dynamics.

To the best of the author's, this study is the comprehensive observational study to thoroughly explore at the same time the variability of the HR on the vertical within a dust plume, the contribution of longwave radiation to the HR and radiative forcing of dust during the night. Past studies analyzing dust-related HR retrievals over the African continent have dealt with column integrated HR retrievals. Over the ocean, Highwood et al. (2003) have provided evidence of the importance of the longwave contribution to radiative heating/cooling associated with dust plumes advected from the continent.

In this paper, we focus on an intense and long-lasting episode of dust being lifted in remote sources in Chad and Sudan and transported across West Africa in the AEJ region. This episode (9–15 June 2006) was well documented in the framework of the AMMA SOP, particularly on 13 and 14 June, when airborne and space-borne lidar data were acquired over some AMMA ground-based instrumental sites in Benin and Niger.

During the daytime, the warming associated with the presence of dust aerosols was found to be between 1.5 K day^{-1} and 4 K day^{-1}, on average, depending on altitude and latitude which is in agreement with previous studies. For instance, Dimri and Jain (1999) found maximum heating rates between 2.2 K day^{-1} in winter and 2.53 K day^{-1} in summer, for dust transport episodes in the Sahara. Also Saha et al. (2008) found heating rates on the order of 3.47 K day^{-1} to be associated with dust events occurring over the French Mediterranean coastal zone. In the present case, strong warming (i.e. heating rates as high as 8 K day^{-1}) was also observed locally in some limited part of the dust. Large vertical gradients of hating rates are also evidenced between the optically thickest and thinnest parts of the plume (up to 3 K day^{-1} km^{-1}). Warming was also observed in the monsoon layer, due to the presence of dust in that layer as well. In cloud-free conditions (over northern Benin and Niger), the HR was observed to scale with the lidar-derived AEC. Over cumulus type clouds (present at the top of the monsoon layer over southern Benin and over the Gulf of Guinea), the largest HRs were

observed just over the cloud. The largest uncertainties on the HR profiles are related to uncertainties on the BER. We also show that in the dust plume, the longwave contribution to the HR is on the order of 40%. Below, in the monsoon layer, this contribution increases to 60–75% near the surface.

During the nighttime, much smaller values of heating/cooling are retrieved (less than $\pm 1\,\mathrm{K\,day^{-1}}$). Furthermore, cooling is observed as the result of the longwave forcing in the dust layer, while warming is observed below the dust layer, in the monsoon layer.

The availability of this information over West Africa thanks to the CALIOP platform will allow in the future evaluating the effect of dust event on the monsoon regime. Thus the next step of this work aims at quantifying the effect of dust over the whole West Africa using CALIPSO data producing three-dimensional maps of radiative forcing for the 9–15 June dust episode. The temporal and spatial variability of dust impact will be scrutinized and analyzed in relationship with the monsoon dynamics. Particular attention will be given to the impact of the transported dust on the dynamic of the AEJ and the modification of the development of westerly African waves through alterations of horizontal temperature gradient.

Acknowledgements. Based on a French initiative, AMMA was built by an international scientific group and is currently funded by a large number of agencies, especially from France, UK, US and Africa. It has been the beneficiary of a major financial contribution from the European Community's Sixth Framework Research Programme. Detailed information on scientific coordination and funding is available on the AMMA International web site http://www.amma-international.org. The authors wish to thank the SAFIRE (Service des Avions Français Instrumentés pour la Recherche en Environnement, www.safire.fr), the Institut Géographique National (IGN, www.ign.fr) and the Division Technique of the Institut National des Sciences de l'Univers (DT/INSU, www.dt.insu.cnrs.fr) for preparing and delivering the research aircraft (Falcon 20/F-GBTM and the ATR42) and the airborne instruments in a timely manner for the AMMA SOP. They also wish to thank the AMMA Operation Center and their partners across West Africa for smoothing out many aspects of the airborne operations. The authors are grateful to D. Bruneau and P. Genau (LATMOS), F. Blouzon, A. Abchiche, D. Chaize, and N. Amarouche (DT/INSU) for re-fitting and operating the LEANDRE 2 system in the F/F20. Special thanks to A. Gribkoff, R. Caillou and M. Laurens (SAFIRE) for operating the dropsonde system, and

to N. Grand (LISA, previously DT-INSU) for operating the AVIRAD system. The authors thank CNRS-INSU for financial support for this publication.

The publication of this article is financed by CNRS-INSU.

References

Alfaro S., Gaudichet, A., Gomes, L., and Maillé, M.: Mineral aerosol production by wind erosion: aerosol particle sizes and binding energies, Geophys. Res. Lett., 25, 991–994, 1998.

Anderson, T. L. and Ogren, J. A.: Determining Aerosol Radiative Properties Using the TSI 3563 Integrating Nephelometer, Aerosol Sci. Technol., 29(1), 57–69, 1998.

Balkanski, Y., Schulz, M., Claquin, T., and Guibert, S.: Reevaluation of Mineral aerosol radiative forcings suggests a better agreement with satellite and AERONET data, Atmos. Chem. Phys., 7, 81–95, 2007, http://www.atmos-chem-phys.net/7/81/2007/.

Berthier, S., Chazette, P., Couvert, P., Pelon, J., Dulac, F., Thieuleux, F., Moulin, C., and Pain, T.: Desert dust aerosol columnar properties over ocean and continental Africa from Lidar in-Space Technology Experiment (LITE) and Meteosat synergy, J. Geophys. Res., 111, D21202, doi:10.1029/2005JD006999, 2006.

Briegleb, B. P, Minnis, P., Ramanathan, V., and Harrison, E.: Comparison of regional clear-sky albedos inferred from observations and model calculation, J. Climate Appl. Meteor., 25, 214–226, 1986.

Bruneau, D., Quaglia, P., Flamant, C., Meissonnier, M., and Pelon, J.: The airborne lidar LEANDRE II for water-vapor profiling in the troposphere, I. System description, Appl. Opt. 40, 3450–3475, 2001.

Chazette, P., Sanak, J., and Dulac, F.: New Approach for Aerosol Profiling with a Lidar Onboard an Ultralight Aircraft: Application to the African Monsoon Multidisciplinary Analysis, Environ. Sci. Technol., 41, 8335–8341, 2007.

Chomette, O.: Modélisation et analyse meso-échelle du cycle de l'aérosol désertique. Aspects radiatifs et dynamiques. Phd thesis, Université de Lille, 1999.

Cuesta, J., Marsham, J. H., Parker, D. J., and Flamant, C.: Dynamical mechanisms controlling the vertical redistribution of dust and the thermodynamic structure of the West Saharan Atmospheric Boundary Layer during Summer, Atmos. Sci. Lett., 10, 1, 34–42, 2009.

Dimri, A. P. and Jain, V. K.: Radiative effect of desert aerosols, Current Science, 77(1), 163–166, 1999.

Dubovik, O., Smirnov, A., Holben, B. N., King, M. D., Kaufman, Y. J., Eck, T. F., and Slutsker, I.: Accuracy assessments of aerosol optical properties retrieved from AERONET sun and sky-radiance measurements, J. Geophys. Res., 105, 9791–9806, 2000.

Dubovik, O., Holben, B., Exk, T., Smirnov, A., Kaufman, Y., King, M., Tanré, D., Slutsker, I.:

Variability of Absorption and Optical Properties of Key Aerosol Types Observed in Worldwide Locations, J. Atmos. Sci., 59, 590–608, 2002.
Fernald, F. G., Herman, B. M., and Reagan, J. A.: Determination of aerosol height distributions by lidar, J. Atmos. Meteor., 11, 482–489, 1972.
Fernald, F. G.: Analysis of atmospheric lidar observations: some comments, Appl. Opt., 23, 652–653, 1984
Flamant, C., Chaboureau, J.-P., Parker, D. P., Taylor, C. M., Cammas, J. P., Bock, O., Timouk, F., and Pelon, J.: Airborne observations of the impact of a convective system on the planetary boundary-layer thermodynamics and aerosol distribution in the intertropical discontinuity region of the West African Monsoon, Q. J. Roy. Meteorol. Soc., 133, 1175–1189, 2007.
Flamant, C., Lavaysse, C., Todd, M., Chaboureau, J. P., and Pelon, J.: Multi-platform observations of a representative springtime case of Bodélé and Sudan dust emission, transport and scavenging over West Africa, Q. J. Roy. Meteorol. Soc., 135, 413–430, 2009.
Formenti P., Grand, N., Chevaillier, S., Schmechtig, C., and Desboeufs, K.: Airborne observations of aerosol particles over western Africa in the summer monsoon season: Spatial and vertical variability of physico-chemical and optical properties, Atmos. Chem. Phys., to be submitted, 2010.
Grams, G., Blifford Jr., I. H., Gillette, D. A., and Russell, P. B.: Complex index of refraction of airbone soil particles, J. Appl. Meteorol., 13, 459–471, 1974.
Heinold, B., Tegen, I., Schepanski, K., and Hellmuth, O.: Dust radiative feedback on Saharan boundary layer dynamics and dust mobilization, Geophys. Res. Lett., 35, L20817, doi:10.1029/2008GL035319, 2008.
Heintzenberg, J., Charlson, R. J., Clarke, A. D., et al.: Measurements and modeling of aerosol single-scattering albedo: progress, problems and prospects, Beitr. Phys. Atmosph., 5(70), 249–263, 1997.
Heintzenberg, J.: The SAMUM-1 experiment over Southern Morocco: overview and introduction, Tellus, 61B, 2–11, 2009.
Highwood, J.E, Haywood, J. M. Silverstone, M. D., Newman, S. M., and Taylor, J. P.: Radiative properties and direct effect of Saharan dust measured by the C-130 aircraft during Saharan Dust Experiment (SHADE): 2. Terrestrial spectrum, J. Geophys. Res., 108(D18), 8578, doi:10.1029/2002JD002552, 2003.
Intergovernmental Panel on Climate Change (IPCC), Climate Change 2007: The Scientific Basis. Contribution of Working Group I to the Third Assessment Report of the Intergovern-

mental Panel on Climate Change, edited by Houghton, J. T., et al., Cambridge Univ. Press, New York, USA, 881 pp. 2007.
Johnson, B.T : The semi direct aerosol effect. Phd thesis, University of Reading, 2003.
Johnson, B. T., Shine, K. P., and Forster, P. M.: The semi-direct aerosol effect: Impact of absorbing aerosols on marine stratocumulus, Q. J. Roy. Meteorol. Soc., 130, 1407–1422, 2004.
Kaufman, Y. J., Tanré, D., Léon, J. F., and Pelon, J.: Retrievals of profiles of fine and coarse aerosols using lidar and radiometric space measurements, Geoscience and Remote Sensing, IEEE Transactions, 41(8), 1743–1754, 2003.
Key, J. and Scheiger, A. J.: Tools for atmospheric radiative transfer: Streamer and FluxNet, Comp. Geosci., 24(5), 443–451, 1998.
Key, J.: Streamer User's Guide. Cooperative Institute for Meteorological Satellite Studies, University of Wisconsin, USA, 96 pp., 2001.
Kim, S.-W., Chazette, P., Dulac1, F., Sanak, J., Johnson, B., and Yoon, S.-C.: Transport and vertical structure of aerosols and water vapor over West Africa during the African monsoon dry season, Atmos. Chem. Phys., 9, 8017–8038, 2009, http://www.atmos-chem-phys.net/9/8017/2009/.
Lebel, T., Parker, D. J., Flamant, C., Bourles, B. , Marticorena, M., Mougin, E., Peugeot, C., Diedhiou, A., Haywood, J. M. , Ngamini, J. B., Polcher, J., Redelsperger, J.-L., and Thorncroft, C. D.: The AMMA field campaigns: Multiscale and multidisciplinary observations in the West African region, Q. J. Roy. Meteorol. Soc., 136, S1, 8–33, 2010.
Messager, C., Parker, D. J., Reitebuch, O., Agusti-Panareda, A., Taylore, C. M., and Cuesta, J.: Structure and dynamics of the Saharan atmospheric boundary layer during the West African monsoon onset: Observations and analyses from the research flights of 14 and 17 July 2006, Q. J. Roy. Meteorol. Soc., 136(S1), 107–124, doi:10.1002/gj.469, 2010.
Mohalfi, S., Bedi, H. S, Krishnamurti, T. N., and Cocke, S. D.: Impact of shortwave radiative effects of dust aerosols on the summer season Heat Low over Saudi Arabia, Amer. Meteorol. Soc., 126, 3153–3167, 1998.
Mueller, D., Mattis, I., Wandinger, U., and Ansmann, A.: Saharan dust over a central European EARLINET-AERONET site: Combined observations with Raman lidar and Sun photometer, J. Geophys. Res. 108, 4345, doi:10.1029/2002JD002918, 2003.
Ogawa, K. and Schmugge, T.: Mapping Surface Broadband Emissivity of the Sahara Desert using ASTER and MODIS data, Amer. Meteorol. Soc., 8(7), 1–14, 2004.

Prospero, J. M., Ginoux, P., Torres, O., and Nicholson, S. E.: Environmental characterization of global sources of atmospheric soil dust derived from the NIMBUS7 TOMS absorbing aerosol product, Rev. Geophys., 40(1), 1002, doi:10.1029/2000RG000095, 2002.

Raut, J.-C. and Chazette, P.: Radiative budget in the presence of multi-layered aerosol structures in the frame of AMMA SOP-0, Atmos. Chem. Phys., 8, 6839–6864, 2008, http://www.atmos-chem-phys.net/8/6839/2008/.

Redelsperger J. L., Thorncroft C., Diedhiou A., Lebel T., Parker D.J. and Polcher J., et al.: African Monsoon Multidisciplinary Analysis: An International Research Project and Field, BAMS, 87, 12 (December 2006), 0E9-1746. 2006.

Saha, A., Mallet, M., Roger, J. C, Dubuisson, P., Piazzola, J., and Despiau, S.: One year measurements of aerosol optical properties over an urban coastal site: Effect on local direct radiative forcing, Atmos. Res., 90, 195–202, 2008.

Satheesh, S. K. V. Ramanathan, V., Holben, B. N., Moorthy, K. K., Loeb, N. G., Maring, H., Prospero, J. M. and Savoie, D.: Chemical, microphysical and Radiative Properties of Indian Ocean Aerosols, J. Geophys. Res., 107(D23), 4725, doi:10.1029/2002JD002463, 2002.

Satheesh, S. K., Deepshikha, S., and Srinivasan, J.: Impact of dust aerosols on Earth-atmosphere clear-sky albedo and its short wave radiative forcing over African and Arabian regions, Int. J. Remote Sens., 27(8), 1691–1706, 2006.

Sokolik, I. N. and Toon, O. B.: Incorporation of mineralogical composition into models of the radiative properties of mineral aerosol from UV to IR wavelengths, J. Geophys. Res., 104(D8), 9423–9444, 1999.

Solmon, F., Mallet, M., Elguindi, N., Giorgi, F., Zakey, A., and Konaré, A.: Dust aerosol impact on regional precipitation over western Africa, mechanism and sensitivity to absorption properties, Geophys. Res. Lett., 35, L24705, doi:10.1029/2008GL035900, 2008.

Stephens, G. L., Vane, D. G., Boain, R. J., Mace, G. G., Sassen, K., Wang, Z., Illingworth, A. J., O'Connor, E. J., Rossow, W. B., Durden, S. L., Miller, S. D., Austin, R. T., Benedetti, A., Mitrescu, C., and CloudSat Science Team: The CloudSat mission and the A-train: A new dimension of space-based observations of clouds and precipitation. Bull. Amer. Meteorol. Soc., 83, 1771–1790, doi:10.1175/BAMS-83-12-1771, 2002.

Stone, R. S., Anderson, G. P., Andrews, E. , Dutton, E. G., Shettle, E. P., and Berk, A.: Incursions and radiative impact of Asian dust in northern Alaska, Geophys. Res. Lett., 34, L14815, doi:10.1029/2007GL029878, 2007.

Tanre, D., Deroo, C., Duhaut, P., Herman, M., Morcrette, J. J., Perbos, J., and Deschamps, P.

Y.: Simulation of the satellite signal in the solar spectrum (5S), Lab. Opt. Atmos., 262 pp., 1986.
Tegen, I., Heinold, B., Todd, M., Helmert, J., Washington, R., and Dubovik, O.: Modelling soil dust aerosol in the Bodélé depression during the BoDEx compaign, Atmos. Chem. Phys., 6, 4345–4359, 2006, http://www.atmos-chem-phys.net/6/4345/2006/.
Tesche, M., Ansmann, A., Müller, D., Althausen, D., Engelmann, R., Freudenthaler, V., and Groß, S.: Vertically resolved separation of dust and smoke over Cape Verde using multi-wavelength Raman and polarization lidars during Saharan Mineral Dust Experiment 2008, J. Geophys. Res, 114, D13202, doi:10.1029/2009JD011862, 2009.
Todd, M. C., Washington, R., Raghavan, S., Lizcano, G., and Knippertz, P.: Regional model simulations of the Bodélé low-level jet of northern Chad during the Bodélé Dust Experiment (BoDEx 2005), J. Climate, 21, 995–1012, 2008.
Tsay, S.-C., Stamnes, K., and Jayaweera, K.: Radiative energy budget in the cloudy and hazy Arctic, J. Atmos. Sci., 46, 1002–1018, 1989.
Voltz, F. E.: Infrared optical constants of ammonium sulfate, Sahara dust, volcanic pumice and flyash, Appl. Opt., 12, 564–568, 1973.
Washington, R., Todd, M. C., Engelstaedter, S., Mbainayel, S., and Mitchell, F.: Dust and the low-level circulation over the Bodélé Depression, Chad: Observations from BoDEx 2005, J. Geophys. Res., 111, D03201, doi:10.1029/2005JD006502, 2006.
Weingartner, E., Saatho, H., Schnaiter, M., Streit, N., Bitnar, B., Baltensperger, U.: Absorption of light by soot particles: determination of the absorption coefficient by means of aethalometers, Aerosol Sci., 34, 1445–1463, 2003.
Welton, E. J., Voss, K. J., Gordon, H. R., Maring, H. , Smirnov, A., Holben, B., Schmid, B., Livingston, J. M., Russell, P. B., Durkee, P. A., Formenti, P., and Andreae, M. O. : Groundbased lidar measurements of aerosols during ACE-2: Instrument description, results, and comparisons with other groundbased and airborne measurements, Tellus Ser. B, 52, 636–651, 2000.
Winker, D., Hunt W., and McGill M.: Initial performance assessment of CALIOP, Geophys. Res. Lett., 34, L19803, doi:10.1029/2007GL030135, 2007.
Young, S., D. Winker, M. Vaughan, Y. Hu, R. Kuehn.: Extinction Retrieval Algorithms, CALIOP Algorithm Theoretical Basis Document PC-SCI-202 Part 4, available on http://www-calipso.larc.nasa.gov/resources/pdfs/PC-SCI-202_Part4_v1.0.pdf, 2008.

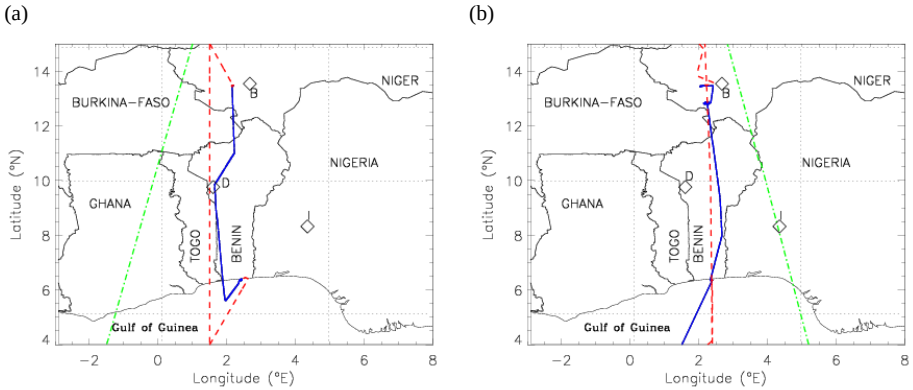

Fig. 1. SAFIRE F/F20 (red dashed line) and ATR-42 (solid blue line) flight tracks on 13 June **(a)** and 14 June **(b)** 2006. Overlain are the CALIPSO tracks (green dash-dotted lines) at 01:37 UTC on 13 June and 14:00 UTC on 14 June 2006. I, D and B correspond to the location of the Ilorin, Djougou and Banizoumbou AERONET stations, respectively.

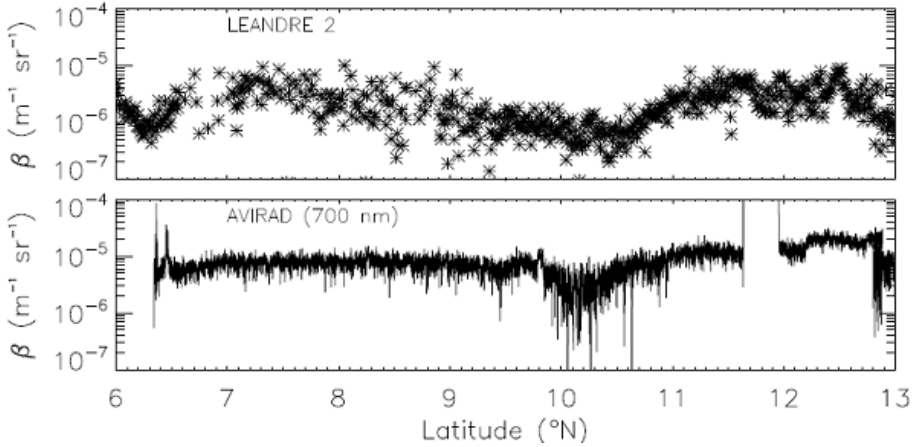

Fig. 2. Backscatter coefficient from LEANDRE 2 at 730 nm (top) and AVIRAD at 700 nm (bottom).

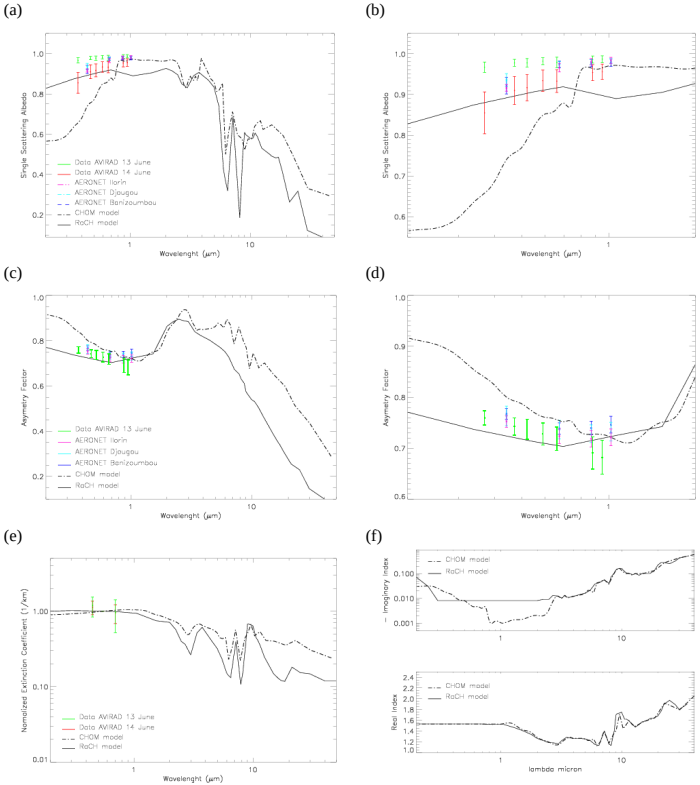

Fig. 3. Wavelength dependence of the single scattering albedo **(a)**, asymmetry factor **(c)**, extinction coefficient normalized at 550 nm **(e)** and refractive index **(f)** from STREAMER (the black solid line corresponds to the RaCH model and the black dashed line to the CHOM model). The red and green symbols correspond to the measurements made by the AVIRAD aerosol sampling device during the 13 and 14 June 2006 ATR-42 flights. AERONET retrievals are in purple (Ilorin), light blue (Djougou) and dark blue (Banizoumbou). **(b)** as in (a) but zoomed between 0.2 and 2 µm. **(d)** as in (c) but zoomed between 0.2 and 2 µm.

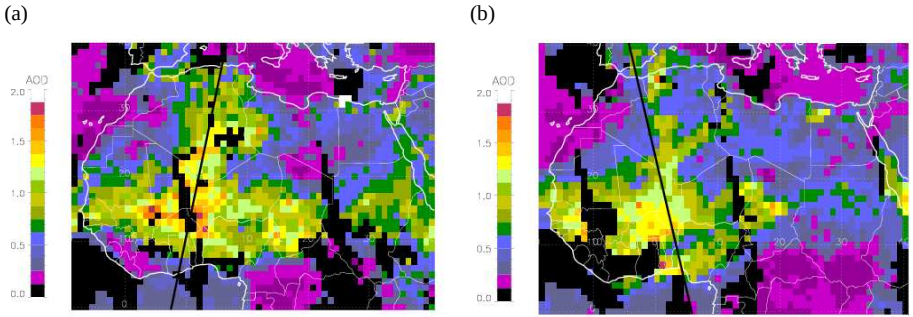

Fig. 4. MODIS-derived AOD over West Africa from 13 June **(a)** to 14 June **(b)** 2006 with CALIPSO tracks (black line).

ACPD
10, 8811–8859, 2010

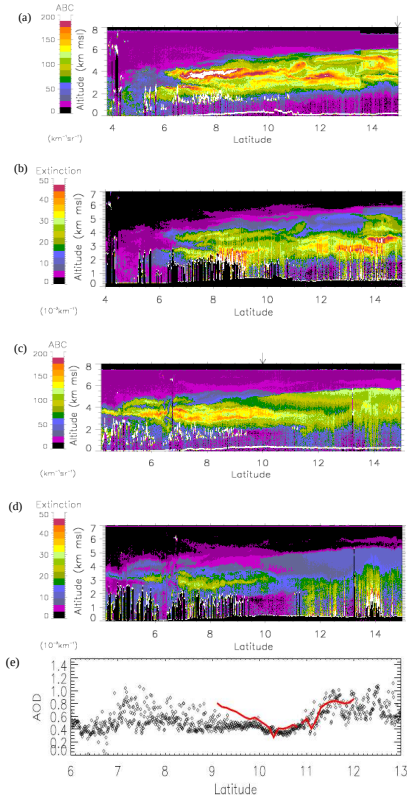

Fig. 5. LEANDRE 2 attenuated backscatter coefficient and LEANDRE-derived extinction on 13 June (**a**, **b**, respectively) and 14 June (**c**, **d**, respectively). Clouds appear as elevated areas of high extinction coefficient (white) on top of regions characterized by reduced extinction coefficients as a result of attenuation between the cloud top and the ground. **(e)** Aerosol optical depth from LEANDRE 2 at 730 nm (diamonds) and MODIS at 670 nm (solid red line).

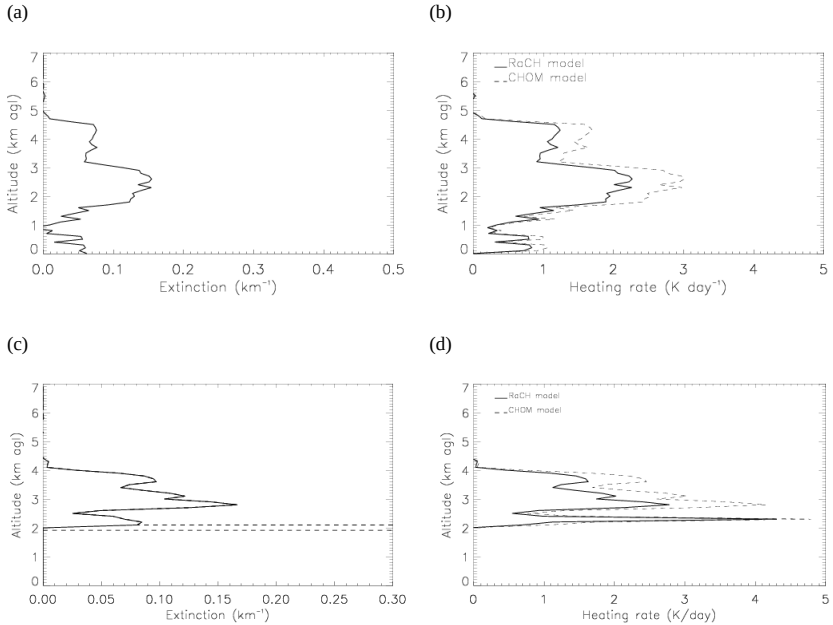

Fig. 6. Lidar extinction at 10° N **(a)** in clear conditions and at 5° N **(c)** in cloudy conditions, and corresponding heating rate **(b, d)** for the 14 June. Dashed line in (c) corresponds to location of the cloud top as derived from LEANDRE 2 measurements.

ACPD
10, 8811–8859, 2010

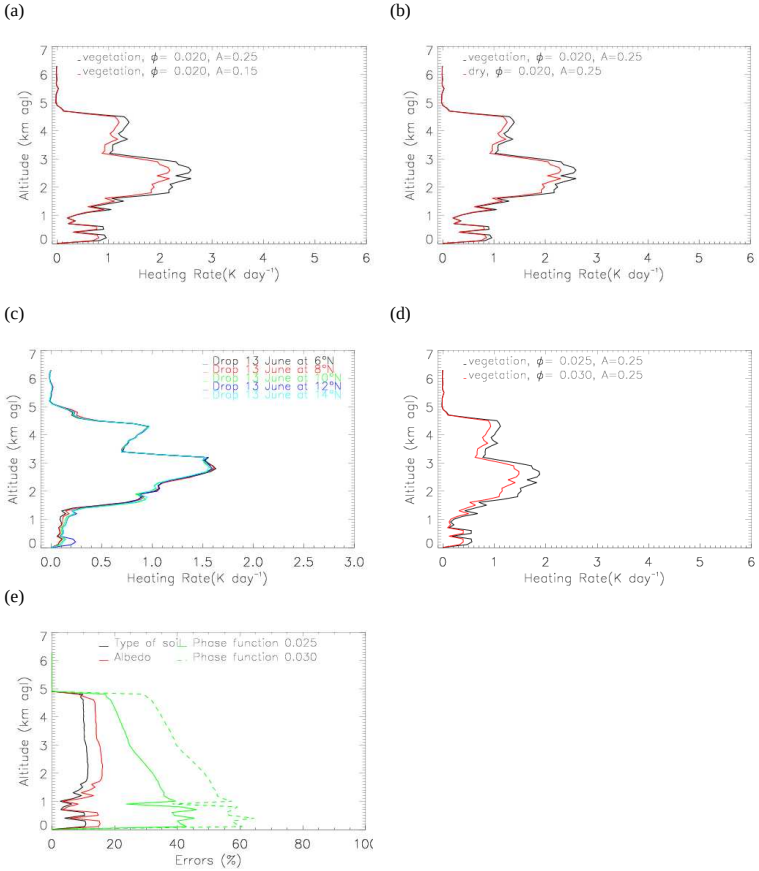

Fig. 7. Sensibility of the LEANDRE 2 –derived heating rate profile at 10° N on 14 June to: **(a)** albedo **(b)** type of soil, **(c)** temperature, pressure and water vapour mixing ratio profiles, and **(d)** dust BER. The profiles of error percentages associated with the sensitivity to each variable is shown in **(e)**. Errors are computed with respect to reference profile shown in Fig. 6b and with RaCH model.

ACPD
10, 8811–8859, 2010

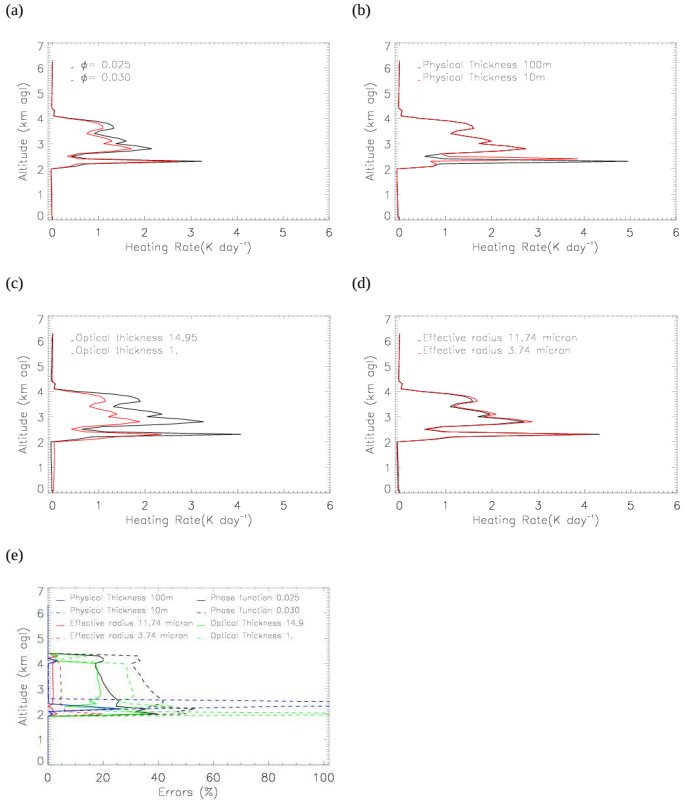

Fig. 8. Sensibility of the LEANDRE 2 – derived heating rate profile at 5° N on June to: **(a)** dust BER **(b)** cloud physical thickness, **(c)** cloud optical thickness and **(d)** effective radius of cloud particles. The profiles of error percentages associated with the sensitivity to each variable is shown in **(e)**. Errors are computed with respect to reference profile with RaCH model shown in Fig. 6d.

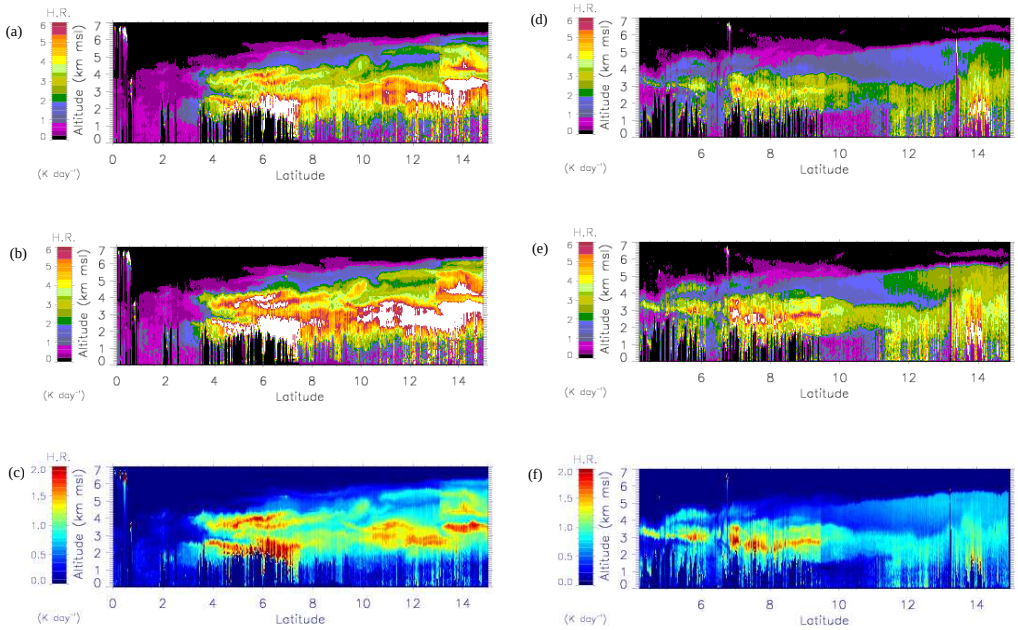

Fig. 9. Heating rate derived from LEANDRE 2 extinction coefficient profiles on 13 June 2006 using the RaCH model **(a)** and the CHOM model **(b)**. **(c)** The difference between the two heating rate fields shown in (a) and (b). **(d)**, **(e)** and **(f)** are as in (a), (b) and (c) but on 14 June 2006.

ACPD
10, 8811–8859, 2010

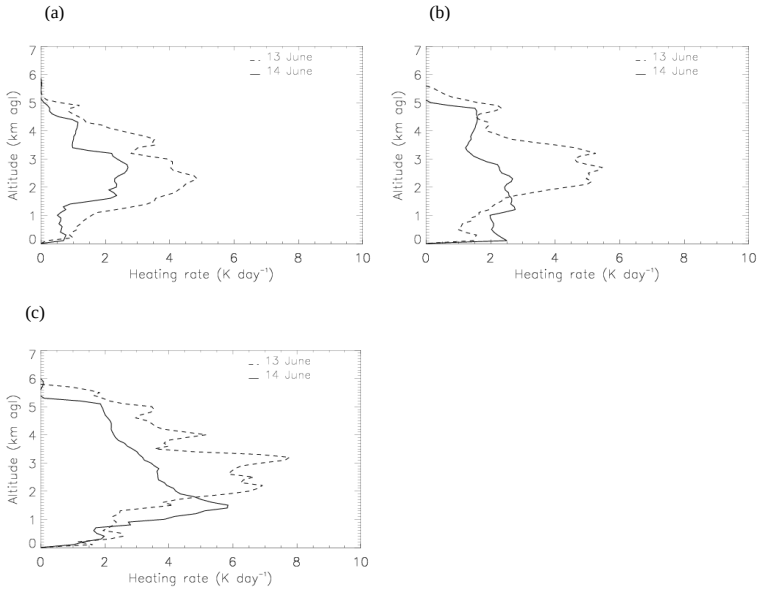

Fig. 10. Heating rate profiles obtained on 13 June (dashed line) and 14 June (solid line) at 10° N **(a)**, 12° N **(b)** and 14° N **(c)** with RaCH model.

ACPD
10, 8811–8859, 2010

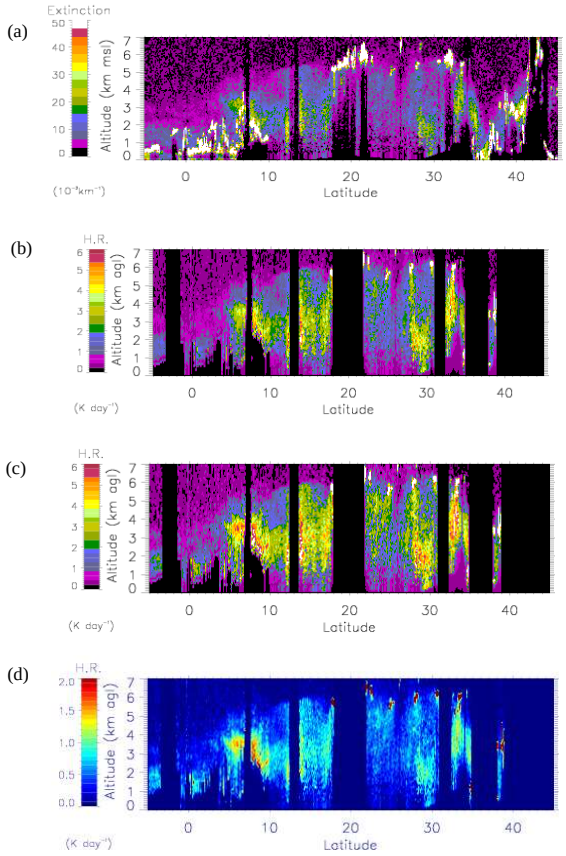

Fig. 11. **(a)** Extinction coefficient profiles derived from the CALIOP lidar on 14 June at 13:20 UTC. Heating rate derived using the RaCH model **(b)** and the CHOM model **(c)**. **(d)** The difference between the two heating rate fields shown in (a) and (b).

ACPD
10, 8811–8859, 2010

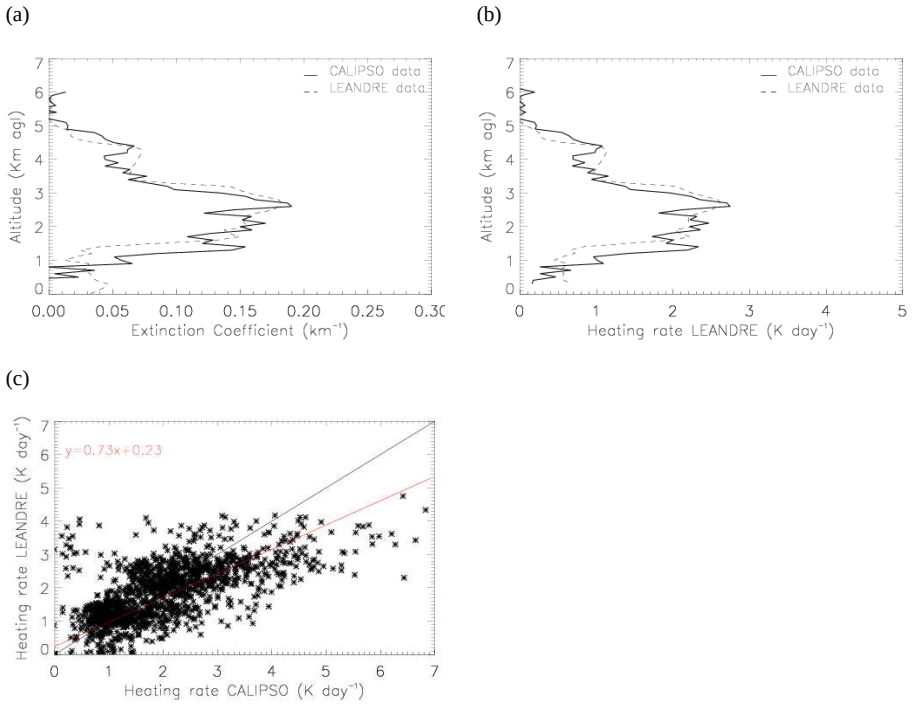

Fig. 12. Comparison of **(a)** extinction coefficient and **(b)** heating rate profiles with RaCH model on 14 June at 12° N derived from LEANDRE 2 (solid line) and from CALIOP dash line. **(c)** Scatter plot of the profile-to-profile comparison of heating rates obtained with LEANDRE 2 and CALIOP between 5° and 15° N. The regression line trough the cluster is given by the solid line.

ACPD
10, 8811–8859, 2010

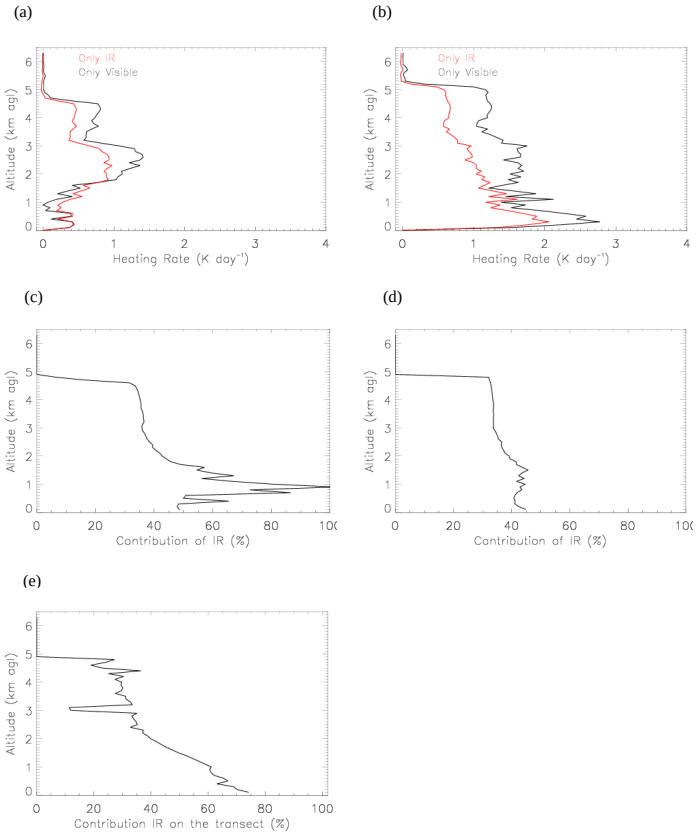

Fig. 13. Heating rate profiles in the infrared (red solid line) and visible (black solid line) at 10° N **(a)** and 13° Ng173 **(b)** with RaCH model. The error made if the infrared contribution is not accounted for in the calculation of the heating rate is shown in **(c)** and **(d)**. **(e)** Contribution of the infrared to the heating rate (in %) for the entire F/F20 transect on 14 June (e).

ACPD
10, 8811–8859, 2010

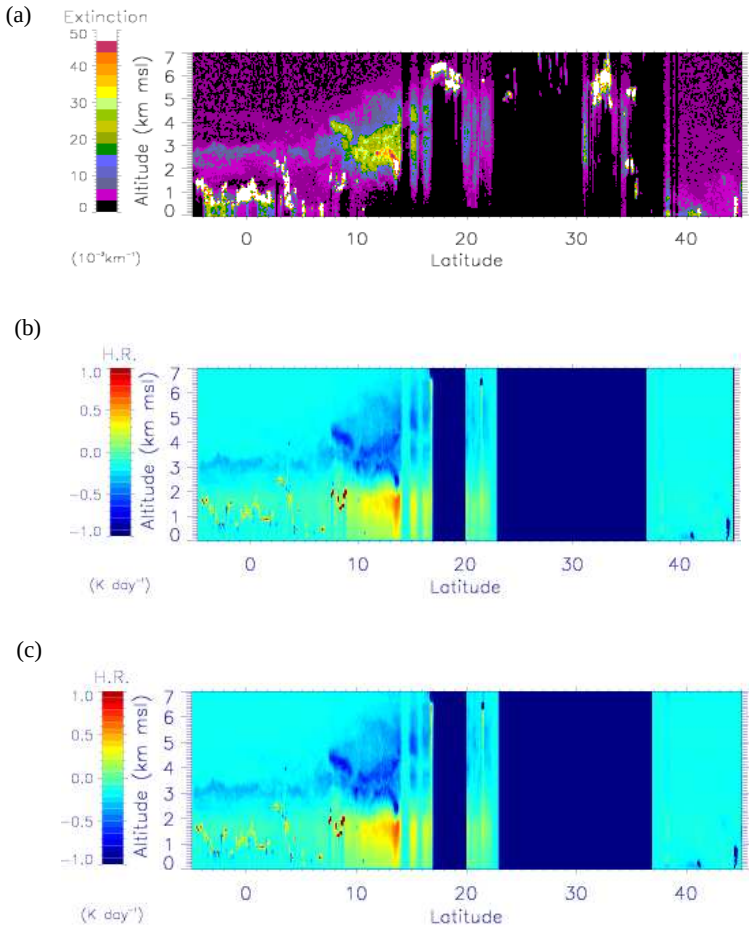

Fig. 14. **(a)** Extinction coefficient profiles derived from the CALIOP lidar on 13 June at 01:39 UTC. Heating rate derived using the RaCH model **(b)** and the CHOM model **(c)**.